Volume 9
Number 11
November 2024
Pages 2821–3062

Reaction Chemistry & Engineering

Linking fundamental chemistry and engineering to create scalable, efficient processes

rsc.li/reaction-engineering

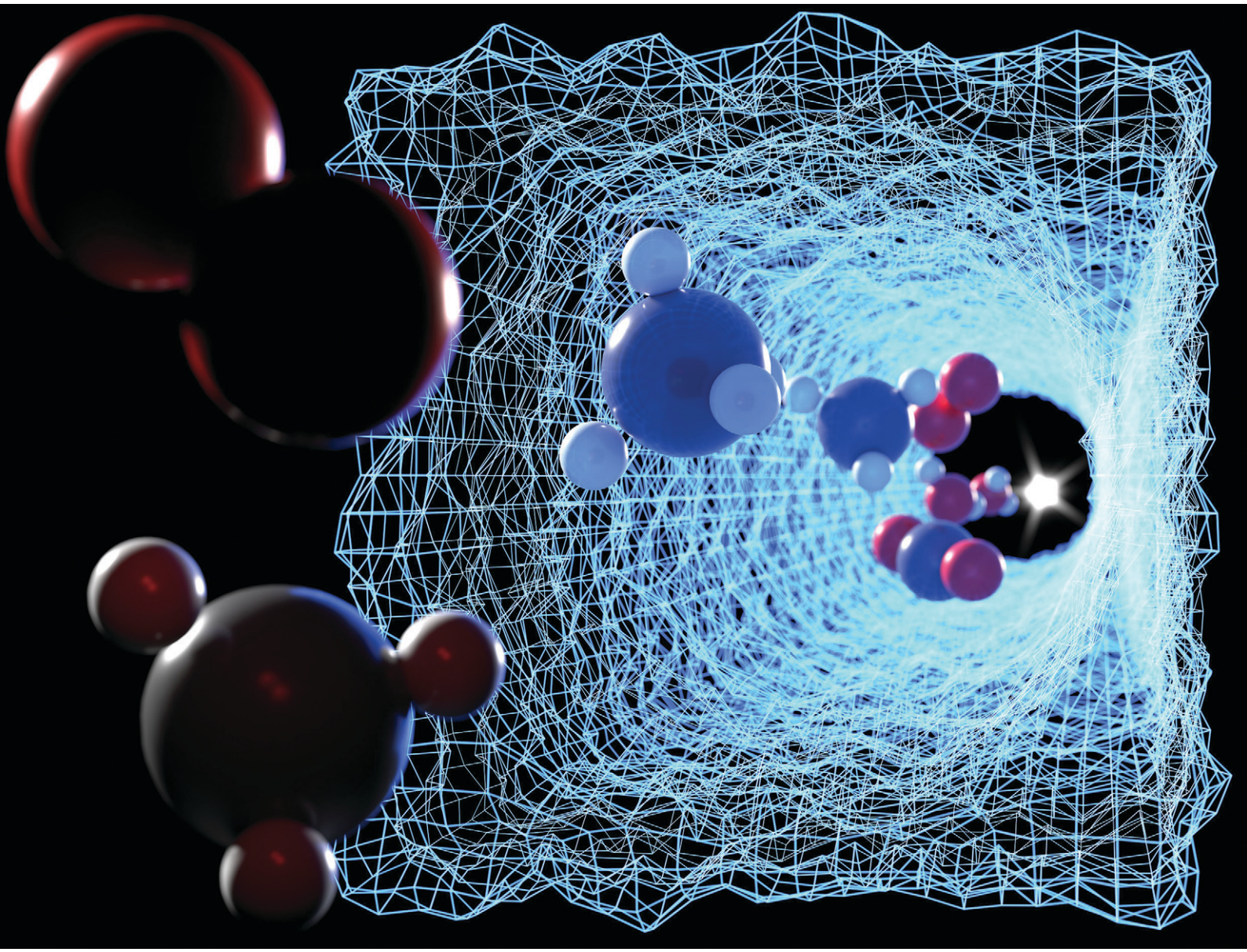

ISSN 2058-9883

ROYAL SOCIETY OF CHEMISTRY

PAPER

Jan-Dierk Grunwaldt *et al.*

A laboratory scale fast feedback characterization loop for optimizing coated catalysts for emission control

Reaction Chemistry & Engineering

ROYAL SOCIETY OF CHEMISTRY

PAPER

View Article Online
View Journal | View Issue

Cite this: *React. Chem. Eng.*, 2024, 9, 2868

A laboratory scale fast feedback characterization loop for optimizing coated catalysts for emission control†

Tim Delrieux, [a] Shweta Sharma,[a] Florian Maurer, [a] Paolo Dolcet,‡[a] Maximilian Lausch, [c] Anna Zimina, [a] Camilo Cárdenas, [a] Patrick Lott, [a] Maria Casapu, [a] Thomas Lennon Sheppard §[a] and Jan-Dierk Grunwaldt *[ab]

Received 28th March 2024,
Accepted 3rd June 2024

DOI: 10.1039/d4re00168k

rsc.li/reaction-engineering

Coating of structured substrates like ceramic honeycombs plays an important role in heterogenous gas-phase catalysis. This work aims at understanding the effects of different coating parameters on the activity of a noble metal-based oxidation catalyst by using a novel fast and non-invasive photo-based channel analysis approach. The impact of the milling intensity, binder amount, catalyst layer thickness and distribution in the ceramic cordierite channels were systematically correlated with the activity profiles for CO, methane and propylene oxidation over a 1.8% Pd/Al_2O_3 catalyst. High milling intensities led to the formation of thinner catalyst layers with smaller particles, which were more evenly distributed throughout all channels and allowed the reactants to penetrate more efficiently. In contrast, the amount of binder added had a negligible influence on the catalyst activity. These findings were validated by X-ray tomography and complemented by SEM-analysis, a diffuse backlight-illumination imaging method, and mercury intrusion porosimetry.

1. Introduction

Structured catalysts such as honeycombs play an important role in many areas of chemical engineering, from the chemical industry to distributed energy conversion and emission control systems for clean air.[1–3] Compared to packed bed reactors, they offer unique advantages such as a high surface to volume ratio, low pressure drop, improved heat and mass transfer properties, and high mechanical and thermal stability.[4–6] Current research areas include clean air applications like mobile and stationary lean-burn natural gas engines in power plants or vehicle exhausts for the abatement of hydrocarbons (HC) or unburnt methane, or in everyday applications like stoves or extractor hoods to reduce emissions of volatile organic compounds (VOCs).[4,7,8] Considering the still intensive utilization of natural gas generators during the energy transition, the use of biogas and biomass, the increased importance of indoor air quality and the increased circularity of carbon-based materials, the demand for structured catalysts will remain high in the future.

To produce such structured honeycomb catalysts, a well-established approach is the so-called catalyst washcoating technology, in which a slurry containing the active phase is deposited on honeycomb-like structures, for example made *via* extrusion of ceramic materials or by additive manufacturing.[9–11] Alternatively, the active phase precursors are added in a second step to a metal oxide washcoated layer. As shown by several studies, the coating process significantly affects both the activity and efficient use of the active phase, as well as the durability of the coated catalyst layer.[12–14] These are typically controlled, starting with the milling of the catalyst powder, adjusting the stability and viscosity of the slurry, the use of binders and stabilizers, application on the substrate, and finally drying and calcination to uniformly distribute and fix the catalyst layer onto the monolith walls.[10,15–18] All these properties are extremely important for applications involving noble metal-based catalysts, due to their scarcity and limited recyclability.[15,19]

[a] *Institute for Chemical Technology and Polymer Chemistry (ITCP), Karlsruhe Institute of Technology (KIT), Engesserstraße 20, 76131 Karlsruhe, Germany. E-mail: grunwaldt@kit.edu*
[b] *Institute of Catalysis Research and Technology (IKFT), Karlsruhe Institute of Technology (KIT), Hermann-von-Helmholtz-Platz 1, 76344 Eggenstein-Leopoldshafen, Germany*
[c] *Institute for Fluid Mechanics and Aerodynamics (SLA), Technical University of Darmstadt (TUD), Flughafenstr. 19, 64347 Griesheim, Germany*

† Electronic supplementary information (ESI) available. See DOI: https://doi.org/10.1039/d4re00168k

‡ Current address: Dipartimento di Scienze Chimiche, Università degli Studi di Padova, Via Francesco Marzolo 1, 35131 Padova, Italy.
§ Current address: Institute of Chemical Technology, Leipzig University, Linnéstraße 3, 04103 Leipzig, Germany.

In the case of methane oxidation, the most active noble metal is Pd.[19–22] Major efforts have been made to understand and improve these catalysts on an atomic level.[19,23] However, on the scale of technical applications, optimization of the structured catalyst as a candidate for the real application is equally important.[24] Aiming for a knowledge-based design is key to reducing the amount of catalyst needed while providing optimal functionality under operating conditions. To pursue such a knowledge-based design, a greater understanding of the effects of specific washcoat characteristics on the noble metal catalyst performance is essential.

In this study, the influence of the slurry formulation on the washcoating and production of a palladium-based structured catalyst was systematically investigated. The focus has been laid on the most crucial parameters, *i.e.* ball milling parameters and amount of binder. The ball milling, on the one hand, is known to greatly influence layer properties such as thickness and porosity, which ultimately affect the transport of the gaseous reactants to the active centers.[25,26] The binder, on the other hand, is crucial for the mechanical stability of the layer during operation: while too little binder can weaken the mechanical stability, too much binder could possibly have a negative influence on the catalytic activity by blocking the active site.[27–29] In general, the catalyst washcoats can be analyzed by established methods such as lab-based or synchrotron X-ray tomography or mercury intrusion porosimetry.[30–36] However, those methods can be costly, time-consuming, and often portray only a small subsection of the produced samples, which is especially true for X-ray nanotomography. Additionally, certain methods can be of an invasive nature, *e.g.* cutting out subsections for tomography, collapsing pore networks or contaminating of the catalyst during to the mercury porosimetry. This often only allows for a post-mortem analysis of the catalyst, or requires the characterization of duplicate samples. For this reason, an in-house developed non-invasive, fast feedback loop is proposed that allows the evaluation of the influence of the different coating parameters directly after drying of the coated catalyst. The findings are validated by X-ray microtomography (μ-CT) and complemented by mercury intrusion porosimetry, rheological measurements, and scanning electron microscopy (SEM). The performance of the catalyst samples was then evaluated during transient catalytic activity tests in a gas feed containing CO, C_3H_6 and CH_4 in 10 vol% O_2/N_2, as these pollutants are typically encountered in environmental catalysis. The gas mixture highlights the activity over a broad temperature range, while the different gases exhibit different diffusion properties and thus help to investigate mass transport limitations.[10,37] Additionally, methane as the most stable alkane is difficult to activate at low temperatures even over noble metal-based catalysts, leading to relevant conversion only at higher temperatures.[38,39]

2. Experimental section

2.1 Catalyst synthesis

A multi-step incipient wetness impregnation was used to prepare a 1.8 wt% Pd/Al_2O_3 catalyst. For this, γ-Al_2O_3 (Puralox TH 100/150, SASOL) was impregnated with an aqueous tetraamminepalladium(II) nitrate solution (5 wt% Pd, abcr GmbH) and dried under atmospheric pressure at 70 °C for 8 h. This step was repeated seven more times until the desired palladium weight loading was achieved. Afterwards the powder was calcined in static air at 500 °C for 5 h. Inductively coupled plasma optical emission spectrometry (ICP-OES) confirmed a weight loading of 1.8 wt% Pd. For the calcined catalyst, a surface area of 129 $m^2\ g^{-1}$ and a pore volume of 0.8 $cm^3\ g^{-1}$ were found by evaluating the N_2-physisorption measurements according to the Brunauer–Emmett–Teller (BET)[40] and Barrett–Joyner–Halenda (BJH)[41] method respectively. The measurements were conducted at −196 °C using an Autosorb iQ (Anton Paar) instrument.

2.2 Slurry preparation and washcoating

The catalyst slurry was based on the mechanical mixture of the pristine catalyst and commercial aluminum hydroxide (Disperal P2, Sasol), which was used as a binder at a dry mass ratio of 10 wt%. In total 8 g of pristine catalyst was added to the formulation. The dry powder was dispersed in water at a mass ratio of 1 : 7. In a first series of experiments, the resulting dispersion was milled two consecutive times for 5 min with different intensities of 100, 200, 300, 500, or 600 rpm. For the second series of slurries the milling intensity was kept constant at 300 rpm and only the amount of binder was varied as followed: 2 wt%; 5 wt%; 10 wt%; 15 wt% and 20 wt%. For milling a ball mill Pulverisette (Fritsch) was used with a chamber volume of 80 mL made from zirconium oxide. The slurry was milled with 75 balls made from zirconium oxide with a diameter of 5 mm. Since the slurry can heat up during milling, the dispersion was allowed to cool down for 15 min between every milling step. Subsequent X-ray diffraction (XRD) measurements showed no milling-induced phase change of the γ-alumina support (Fig. S1†). The resulting particle sizes in the slurry have been measured with the diffuse backlight-illumination imaging method.[42,43] Afterwards, the pH-value of the slurry was adjusted with nitric acid to a pH = 3 in order to improve the colloidal stability. The complex viscosities of the slurries were measured by an ARES G2 device (TA Instruments) with amplitude sweeps. The prepared slurry was then used for dip coating. A cordierite honeycomb monolith (NGK, 600 CPSI, 3.5 mil) of cylindrical shape with a length of 5 cm and a diameter of 2.54 cm resulting in a volume of 25.3 mL was used as a substrate. A schematic drawing of the washcoating process is depicted in Fig. 1.

The cordierite monolith was fully immersed in the slurry and then withdrawn. The excess liquid in the honeycomb was removed by pressurized air and the honeycomb was dried with a heat gun set to a temperature of 370 °C (approx.

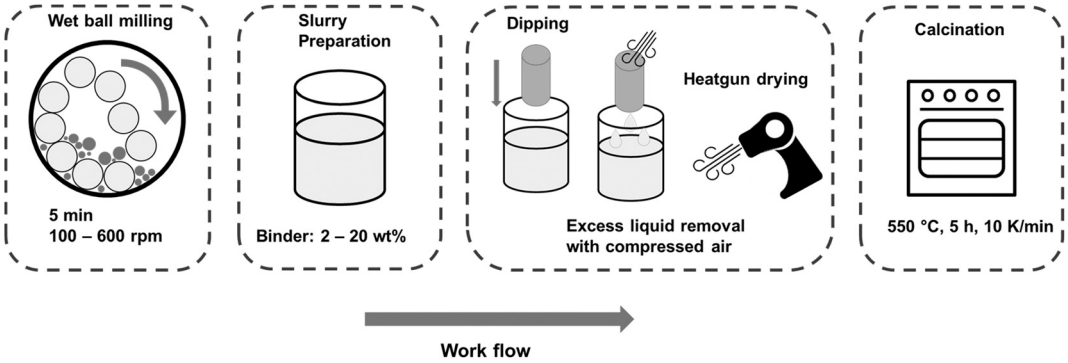

Fig. 1 Workflow of the monolithic honeycomb preparation. Starting with mixing the dry ingredients and then adding water in the ratio of 1 : 7 to the dry mass. Subsequently, the dispersion is milled with different intensities. The resulting slurry is used for coating the monolithic honeycombs until the desired loading is achieved. Lastly, the honeycombs are calcined in static air for 5 h at 550 °C.

2 cm away from the sample position). After each coating step the honeycomb was flipped to ensure an equal coating. The coating process was repeated until the desired Pd loading of approximately 80 g_{Pd} ft^{-3} was reached, resulting in 15–17 dips. Finally, the honeycomb was calcined in static air for 5 h at 550 °C. The porosity of the different samples was measured by mercury intrusion porosimetry (MIP) (Micromeritics, United States) in a pressure range from 0.2–4200 bar. Additionally, in order to measure the mechanical stability of the washcoat, the samples were submerged in a 1 : 1 mixture of water and isopropanol and put into an ultrasonic bath for 5 min. At the end of this procedure, the samples were dried and afterwards weighted.

2.3 Catalytic methane oxidation under transient conditions in the presence of CO and propylene and spatial profiles

Transient catalytic tests were performed using two different gas hourly space velocities (GHSV) of 30 000 and 50 000 h^{-1}. As described in detail earlier,[44] the catalyst coated honeycombs (5 cm length, 2.54 cm width, 73–84 g ft^{-3} Pd loading) were fixed in the reactor, (2.6 cm inner diameter, 65 cm length) with quartz glass wool in order to avoid the bypass of reactants during testing. The applied gas feed (1000 ppm CO, 500 ppm C_3H_6, 3000 ppm CH_4, 10% O_2 in N_2) was set on a bypass line before it was fed to the reactor and heated from 110 °C to 550 °C with a heating rate of 5 °C min^{-1}. Once reaching 550 °C, the temperature was kept constant for 10 min and cooled down afterwards with 5 °C min^{-1} to 110 °C. Two consecutive light-off experiments were performed, with the first one serving as a degreening step. At the reactor outlet, the gas composition was analyzed with a Fourier-transform infrared spectrometer (FTIR, MG2030, MKS Instruments). Additionally, for two samples spatial profiles of the methane conversion along the honeycomb channel were measured in a spatial profiling setup (SpaciPro setup[45,46]) described in detail previously. The gas feed (3000 ppm CH_4, 10% O_2 in Ar) for these measurements was adjusted to a GHSV of 30 000 h^{-1}. The effluent gas stream was analyzed by an FTIR spectrometer (MG2030, MKS Instruments). The spatially resolved CH_4 concentration profiles were obtained by moving a quartz glass capillary (outer diameter 170 μm, inner diameter 100 μm) through the corner of a single central channel of the coated monolith. For this purpose, samples were collected every 2 mm along the channel using a mass spectrometer (HPR20, Hiden Analytical). The sampling frequency of the mass spectrometer was 1 Hz and each capillary position was sampled for more than 5 min.

2.4 X-ray tomography

X-ray computed tomography (XCT) measurements were conducted using a ZEISS Xradia Versa 520 X-ray microscope (Oberkochen, Germany). Selected honeycombs cut to the size of 3 × 3 channels with a length of 1 cm were analyzed with a 4.0× objective lens in binning 2 mode using a tungsten X-ray source. The measurements were performed at 50 kV and 80 μA for an optimized transmission and signal to noise ratio. These settings resulted in a magnification of 3.94 and a voxel size of 4.55 μm. 1000 projections were taken over an angular range of 360° with an exposure time of each 1 ms. The total measurement time per honeycomb was about 3 h. A representative three-by-three 1 cm piece at the inlet position were measured for each sample.

2.5 Photo-based analysis

In order to create a non-destructive, fast and reproducible way to analyze the thickness as well as the quality of the coating within the honeycomb channels we developed a non-invasive photo-based channel analysis. Pictures of the honeycomb in- and outlet were taken with a single-lens reflex (SLR) camera (EOS-2000D, Canon), having a lens with a focal length of 55–250 mm (EF-S 55–250 mm, Canon). All pictures were taken with a constant sample to camera distance of 75.5 cm and the objective was set to 250 mm to minimize the angle of view. Additionally, a ring light was placed behind the camera resulting in an even lighting. The resulting pictures were processed using the Fiji software package[47] according to the scheme in Fig. 2. The results of the image processing

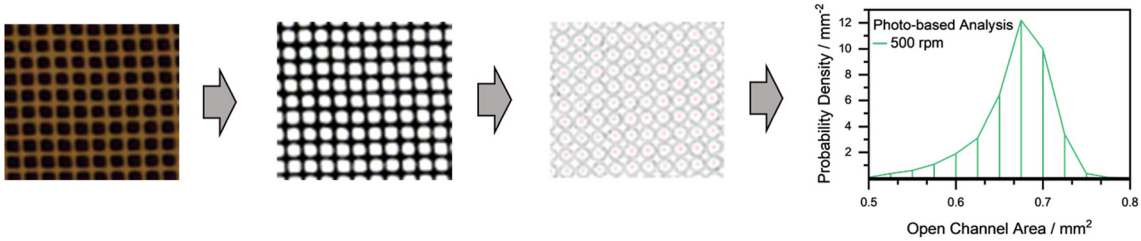

Fig. 2 Overview on the workflow to gain information on the layer thickness and its distribution from the photo analysis: after taking a picture of the in-/outlet of the honeycomb (on the left), the threshold is adjusted, which helps to identify the channels as particles. The area of the particles is then measured by the "analyze particles…" function in Fiji which results in the density distribution that correlates with the open channel areas (depicted on the right).

shows the distribution of the open channel area (OCA) of the investigated honeycombs.

3. Results and discussions

3.1 Characterization of the layer thickness

An optimal washcoated monolith comprises an as thin as possible catalyst layer to minimize pressure drop and internal diffusion limitations (~100 μm) while maintaining its porosity[34,48,49] and a sufficient catalyst loading.[34,48,49] In this way the gas can penetrate the entire catalyst pore network, as thin layers and small pores form a short diffusion length. In order to probe the influence of the layer thickness, both the ball milling intensity and binder concentration were varied during slurry preparation as described above. However, the setting of 100 rpm did not allow to coat the honeycomb without fully blocking the channels. For the quantification of the coating homogeneity and layer thickness, X-ray μ-CT is an established characterization method.[32–34,50] X-ray CT has a key advantage by providing 3D spatially-resolved information about the axial distribution of the catalyst within the channels of the monolith, which cannot be obtained using other methods. In this study, X-ray μ-CT was not only used to analyze the layer thickness as a function of axial position, but also to validate the open channel area (OCA) from the developed photo-based channel analysis. In general, maintaining an overall high OCA is particularly important to avoid back-pressure issues for applications where a high GHSV is used. For this purpose, the selected samples prepared with a ball milling intensity of 200, 300 and 500 rpm as well as samples with 2 wt% and 20 wt% binder concentration have been first analyzed by the X-ray μ-CT. Fig. 3 shows a typical X-ray μ-CT image of the samples prepared by milling the slurry at 200 and 500 rpm. Starting with the comparison of the variation in the milling intensity, in Fig. 3b) it can be observed that at 200 rpm thicker catalyst layers are formed, which seem to be unevenly distributed along the analyzed channels, and showing larger pores at the given resolution of 10 microns. As shown in Fig. 3a), the 500 rpm sample exhibits significantly thinner catalyst layers, which is more evenly distributed along the channels of the honeycomb. These layer thicknesses are inversely proportional to the OCA of the different samples, with higher OCA values translating to thinner catalyst layers and *vice versa*. Fig. 3c) shows an overview on the relationship between the layer thickness (left axis) and OCA (right axis) as a function of the milling intensity: the layer thickness becomes smaller and the OCA larger when varying the milling intensity from 200 rpm to 500 rpm. With an average

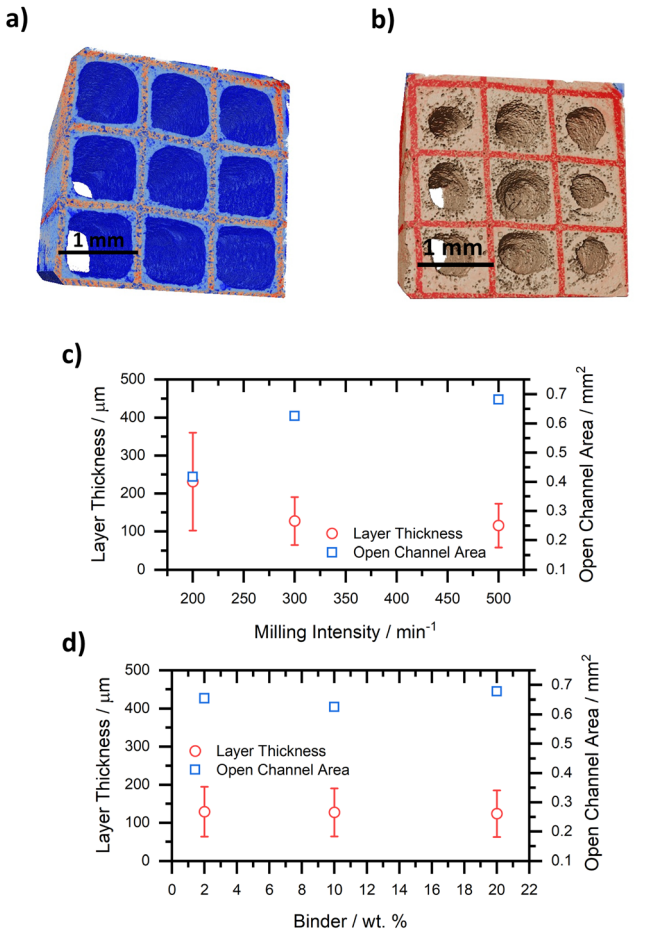

Fig. 3 Characterization of the monolithic honeycombs. a) Example for a 3D X-ray μ-CT image of 500 rpm sample and b) selected 3D X-ray μ-CT image of 200 rpm. c) Total OCA derived from X-ray μ-CT of the different samples plotted against the applied milling intensity with constant 10 wt% added binder and d) OCA of the different samples plotted against the used binder concentration with constant milling intensity of 300 rpm.

thickness of 230 ± 129.19 μm over the whole tomogram, the catalyst layer for the 200 rpm sample is approximately twice as thick as that of the 500 rpm sample, which is only 115 ± 57.4 μm. The corresponding OCAs are 0.42 mm^2 and 0.68 mm^2 respectively. As shown in Table 1, the different catalyst amounts deposited on the honeycombs vary only slightly by up to 9% from the initial target of 80 g ft^{-3}, which cannot be the cause for the major variation in the layer thickness.

Fig. 3d) reports the differences in the catalyst layer thickness and OCA as a function of the binder concentration in the slurry for a constant milling intensity of 300 rpm. Also, in this case, the total amount of catalyst and binder coated on the substrate was maintained at similar values (variation of 9% between the sample containing 2 wt% and that containing 20 wt% binder). In contrast to the effect of the milling intensity, it can be observed that the amount of binder only has a minor influence on the catalyst layer thickness and OCA. Hence, the catalyst layer thickness seems to be predominantly affected by the applied milling intensity.

In a next step, the observed effects of the milling intensity and binder concentration were further investigated by the photo-based channel analysis method. Moreover, the samples obtained at 100 rpm and 600 rpm milling intensity, and with 5 wt% of binder content were evaluated as well. Pictures of the honeycomb in- and outlet were taken and the density distribution of the OCA was systematically analyzed. The resulting pictures were processed by adjusting the threshold to obtain black and white images, from which the Fiji software was able to directly calculate the open channel area. This method allowed the evaluation of every single sample rapidly and directly in the lab after its production. Furthermore, higher statistics could be gained since all monolith channels were included in the final assessment. Also, by limiting the range of detected open channel areas, noise or broken and clogged channels could be excluded or identified. The only disadvantage was that the distribution along the channels could not be checked without damaging the sample.

Fig. 4a) shows the density distribution of the open channel area for the samples obtained with 200, 300 and 500 rpm milling intensity, as well as the OCA of the samples containing 2 wt%, 5 wt% and 20 wt% binder. A lower OCA density corresponds to thicker catalyst layers while a higher one represents thin catalyst layers. The 200 rpm sample exhibits a wide distribution, which has a maximum at around 0.6 mm^2. However, a pronounced tail towards smaller values is visible, indicating the presence of thicker layers. The OCA distribution of the 300 rpm catalyst is also cantered around 0.6 mm^2, but the tail is less pronounced compared to the 200 rpm sample, indicating a more homogeneous coating if ball milling is conducted at 300 rpm. The 500 rpm sample shows a shift towards higher values around 0.7 mm^2, with a very small tail at smaller OCA density, which corresponds to the thinnest layer among all investigated samples, as well as to a homogeneous distribution across the channels. In analogy to the X-ray μ-CT-derived data shown in Fig. 3c), Fig. 4b) shows the OCA as a function of milling intensity based on the photo-analysis data. Here, a rather identical trend can be observed, showing that the photo-based channel analysis is in good agreement with the results of the X-ray μ-CT study. The small differences can be explained by different statistics of the two methods. While X-ray μ-CT in this case only shows the catalyst layer in 9 monolith channels and their axial distribution, the photo-based channel analysis represents roughly 450 channels for a 600 cpsi monolith as subject to the present study, with the possibility to even increase the size of the monolith. Furthermore, the evaluation of the 100 and 600 rpm sample with the photo-based channel analysis fits to the trend observed by X-ray μ-CT as well. Fig. 4c) depicts the OCA as a function of binder concentration. Again, the same trend as derived from the X-ray μ-CT investigations is observed, indicating that the binder concentration only has a minor influence on the layer thickness. As already mentioned above, this resulting area is then directly proportional to the coating thickness. Additionally, the width of the OCA distribution offers the possibility to draw conclusions on the homogeneity of the coating.

Overall, the photo-based channel analysis therefore offers the opportunity to provide a rapid feedback loop on the changes in the catalyst layer due to the variation in the slurry preparation parameters, which can directly be tracked in the laboratory. This facilitates the improvement of the washcoating process in a rational way and, in future, can assist the design of even more complex structures such as dual layer or zone coatings. However, the photo-based channel analysis only allows an investigation at the inlet and outlet and is currently especially suited for single layer coatings. In order to estimate the reliability of the data, we compared the 2D information obtained *via* the photo-based analysis with 3D X-ray μ-CT data collected along the monolith channels (Fig. 5) for a catalyst sample milled with 500 rpm and containing 10 wt% binder. For this milling intensity, a similar OCA distribution is recognized along the coated catalyst by the photo-based analysis method. This outcome emphasizes once again high potential of this easily accessible evaluation method to characterize series of catalyst coated samples in a rapid and reproducible way. In case of double layer coatings the technique should be applied after both coating procedures (*i.e.* the first one and then the second one, should also be verified by complementary techniques).

Table 1 Overview on the variation of milling intensity and binder on the uptaken catalyst mass (without binder) and resulting catalyst loading

Milling intensity/rpm	Binder/wt%	Catalyst mass w/o binder/g	Catalyst loading/g_{Pd} ft^{-3}
200	10	3.7	73
300	10	3.9	78
500	10	4.1	82
300	2	4.3	86
300	5	4.3	86
300	20	3.7	74

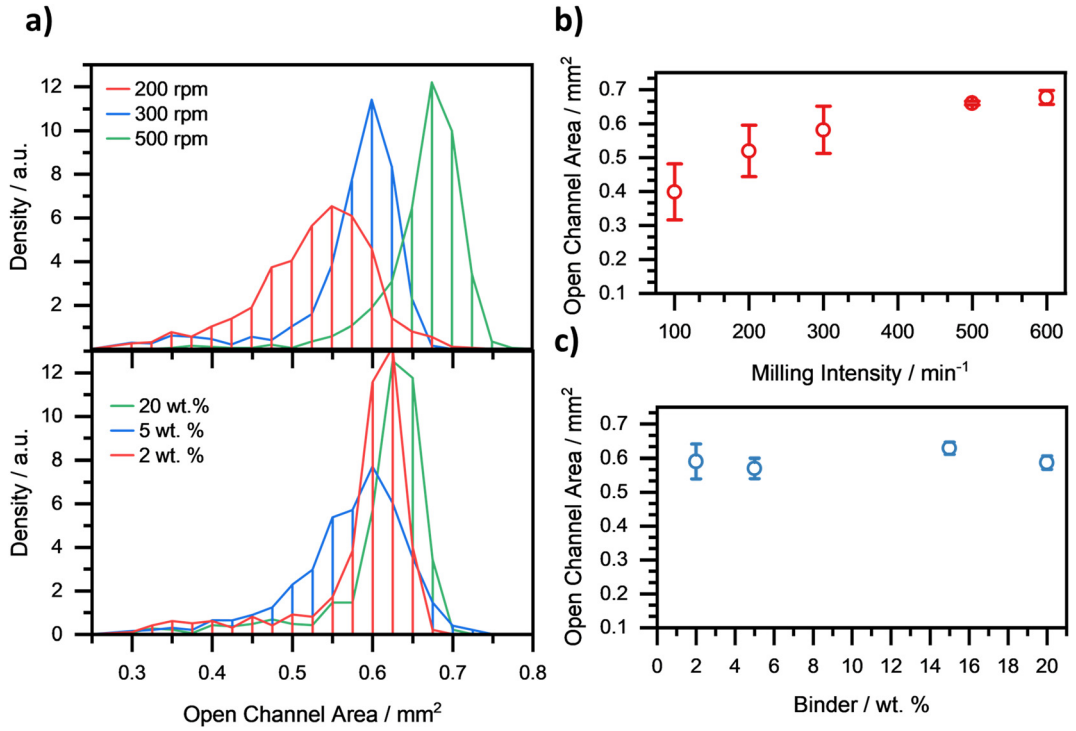

Fig. 4 Resulting open channel areas of the photo analysis. a) Distributions of OCA depending on the milling intensity showing larger OCA for higher intensities indicating thinner catalytic layer and OCA distributions as a function of the added binder indicating a similar OCA for all variations. b) The median of the open channel areas plotted against the corresponding milling intensity. c) Median of OCA as a function of the added binder, further indicating a minor influence to the layer thickness.

3.2 Influence on the layer formation

In addition to the catalyst layer thickness and distribution, parameters such as grain/particle size and porosity are known to have a major impact on the catalytic performance of structured catalysts. In our study the particles size was evaluated as a function of milling intensity by using the diffuse backlight-illumination imaging method. Additionally, rheological studies of various slurries, mercury intrusion porosimetry of the catalyst coated samples, and SEM-analysis of the catalyst layer have been employed. Fig. 6a) shows particle size distributions as obtained by the diffuse backlight-illumination imaging method for the samples prepared at 200, 300 and 500 rpm milling intensity and the corresponding median support particle size. It has to be noted that the detection limit of the method is 5 μm. Nevertheless, the method can be utilized to derive a correlation of particle size and milling intensity. By applying a milling intensity of 200 rpm a very wide distribution with a maximum particle size of up to 30 μm is obtained. The corresponding median particle size is 7.2 μm, making it the largest in the investigated series. Note that further agglomeration cannot be excluded during the coating process. Upon applying 300 rpm the sample exhibits a narrower particle size distribution, with a corresponding median particle sizes of 6.7 μm. Additionally, no particles larger than 20 μm can be observed. At 500 rpm the narrowest distribution is obtained, with a corresponding particle size of 6.0 μm and no particles larger than 15 μm. In addition, a sharp peak for 5 μm sized particles can be observed, which indicates the presence of higher amounts of smaller particles. The size of the dispersed particles is critical for the stability of the slurry, as too large particles will sediment not only during the monolith dipping process, but also during the drying step.

Fig. 6b) displays the measured complex viscosity as a function of the different applied process parameters. The curve obtained for the 200 rpm sample (red) indicates that no equilibrium can be reached during the measurement and that the complex viscosity increases with every measurement cycle. This is likely due to sedimentation of the slurry during the measurement cycles, which is supported by the diffuse backlight-illumination imaging method data that confirmed the presence of larger particles that sediment faster than smaller particles. The reason for the increase in intensity can be explained by the fact that the measurement was conducted in the lower quarter of the vessel, where the slurry accumulates and the viscosity increases. A similar behavior is observed for the 300 rpm sample, but not to the same extent as for the 200 rpm sample. In this case the first two measurement cycles reach equilibrium; only during the third measurement an increase in viscosity can be observed, indicating the colloidal instability of the slurry. The complex viscosity of the 500 rpm sample reaches equilibrium for all measurement cycles performed, which does not only demonstrate the stability of the slurry, but also gives a value

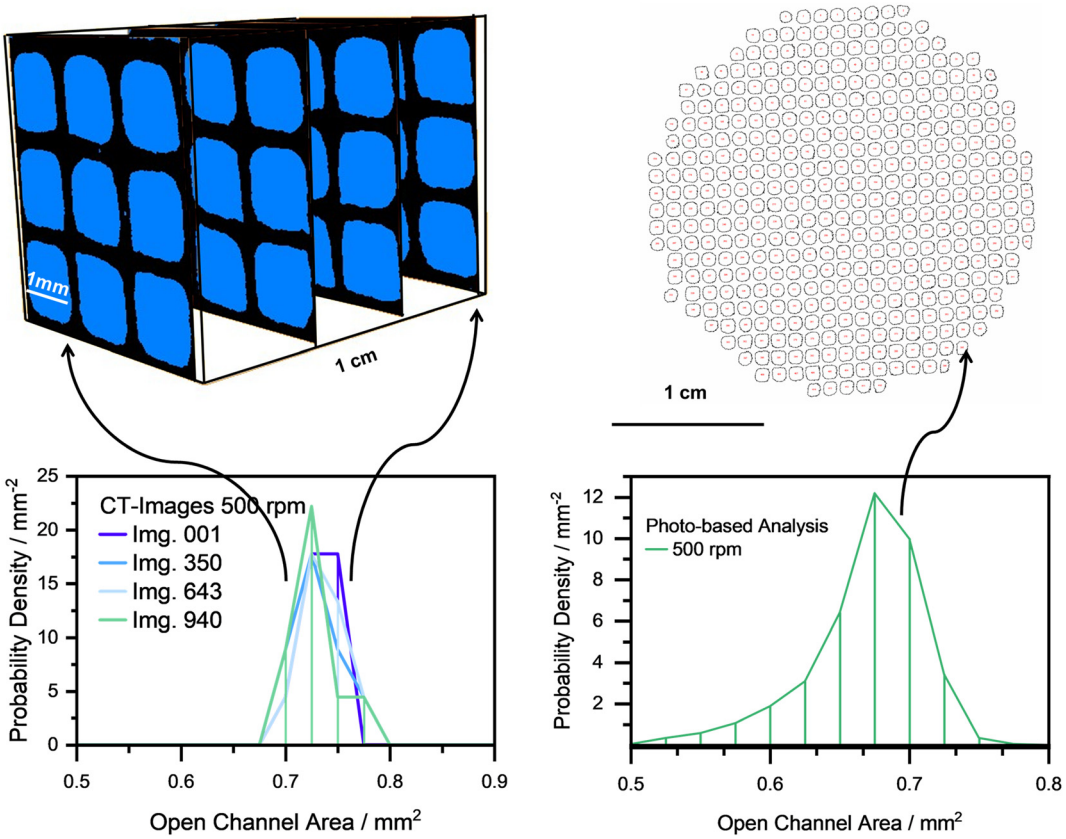

Fig. 5 Direct comparison of open channel area (OCA) derived from μ-CT (schematic drawing) and photo-based analysis, underscoring how the photo-based analysis can serve as descriptor for the quality of the coating.

for the complex viscosity of 0.002 Pa s, which is roughly twice as high than that of water at 20 °C. This observation is in line with the observed particle size of 6.6 μm on average, which makes the sedimentation a slower process compared to the slurries milled with lower rpm. For the addition or removal of the binder no influence on the viscosity could be found (Fig. S3†).

Fig. 6c) shows the resulting pore size distribution as a function of the milling intensity and for the uncoated monolith. The uncoated monolith has a distinct peak that correlates to a median pore size of 7.39 μm. The results reported in Table 2 show that with increasing milling intensity the overall porosity remained similar, whereas the median pore size strongly decreases. The coated samples exhibit a bimodal distribution of the pores, hence for both peaks a median value was calculated. Fig. 6c) depicts the distribution of the pore sizes over the logarithmic differential pore volume. For all samples (bare monolith excluded) a bimodal distribution is observed.

The peak around 7–8 μm can be assigned to the pores of the uncoated monolith, while the peak at 0.02 μm can be assigned to the formed catalytic layer and the alumina support. In the case of the 300 and 500 rpm samples, it can be observed that the uncoated monolith peak is shifted to the left, which suggests a filling of the pore structures of the uncoated monolith as well as the formation of the macroporous layer. This could be further investigated with cross section SEM or high resolution X-ray tomography, *e.g.* ptychographic X-ray computed tomography.[36,51] This is in line with the observation from the diffuse backlight-illumination imaging method, in which smaller particles were found for the 300 and 500 rpm samples, which also influence the macroporous layer and are detrimental to the effective diffusivity and the overall performance. However, a change in porosity of the alumina particles is not expected. Fig. 6d) shows the corresponding SEM-analysis of the produced layers for the 200 rpm, 300 rpm and 500 rpm sample. The image for the sample obtained at 200 rpm displays large particles, which show distinct grain boundaries between them, forming larger pores that are also visible in the X-ray μ-CT images and the MIP (Fig. 3 and 6, respectively). The 300 rpm and 500 rpm samples, on the other hand, show coherent layers with small cracks which can improve the effective diffusivity trough the coating.[51] Only a small number of grains of smaller sizes are visible for both samples.

Additionally, as seen in Fig. S2† the amount of added binder strongly influences the mechanical stability. The addition of higher amounts of binder lead to an overall higher mechanical stability. All in all, the combination of different characterization techniques has been shown to be important as it helps to better understand the parameters

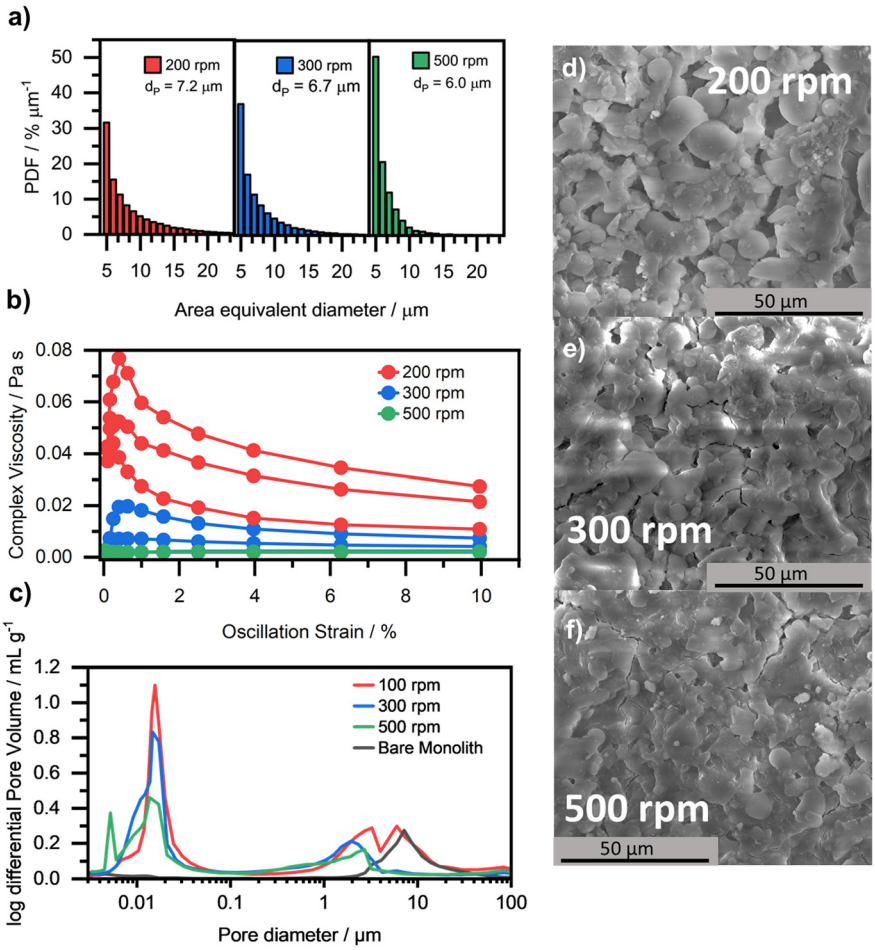

Fig. 6 Particle sizes of the Pd/alumina particles in slurry and after deposition. a) Probability density function (PDF) as a function of different milling intensities measured by the diffuse backlight-illumination imaging method. b) Rheological measurements of slurry with varying milling intensity and a constant 10 wt% binder. c) Pore size distribution of samples with different milling intensities and constant 10 wt% binder. d) SEM-image of catalyst layer that has been milled with 200 rpm; large particles are observed and no coherent layer. e) SEM-image of catalyst layer that has been milled with 300 rpm showing a coherent layer. f) SEM-image of catalyst layer that has been milled with 500 rpm forming a coherent layer consisting of small particles.

influencing the catalyst layer formation. In particular, the diffuse backlight-illumination imaging method can supplement the non-invasive photo-analysis procedure, since both are fast and cheap techniques, therefore contributing to a rapid feedback loop on structured catalyst preparation. The measurements have shown that a higher milling intensity of 500 rpm leads to smaller particles, which form a stable slurry with an increased initial viscosity. During the washcoating process, the small particles can penetrate the pore system of the ceramic honeycomb. Moreover, due to the stability of the obtained slurry, a uniform and coherent coating is obtained. The catalyst layer exhibits small pores and a porosity of 53%, which allows the gas to efficiently penetrate while providing a short path to the active centers of the catalyst. In contrast, ball milling the slurry with 200 rpm results in a sample that exhibits large particles that are prone to sedimentation. Washcoating of monoliths with such a slurry creates a pore network of large pores, thick catalyst layers and a small OCA, which increase the back-pressure, diminish the catalyst efficiency.

Table 2 Porosity and median pore diameter as a function of milling intensity and as reference also for the bare uncoated monolith

Milling intensity/min^{-1}	Porosity/%	Median pore diameter/µm
Bare monolith	27	7.4
100	58	0.016/4.0
300	55	0.011/2.9
500	53	0.013/1.9

3.3 Influence on the catalytic activity

In addition to developing a reliable and fast quality control of the produced monolithic catalyst sample, it is equally important to correlate the catalyst layer properties to the catalytic performance, *i.e.* to obtain a catalyst that provides sufficient catalytic activity over a broad temperature range and a range of operating conditions. As a test reaction,

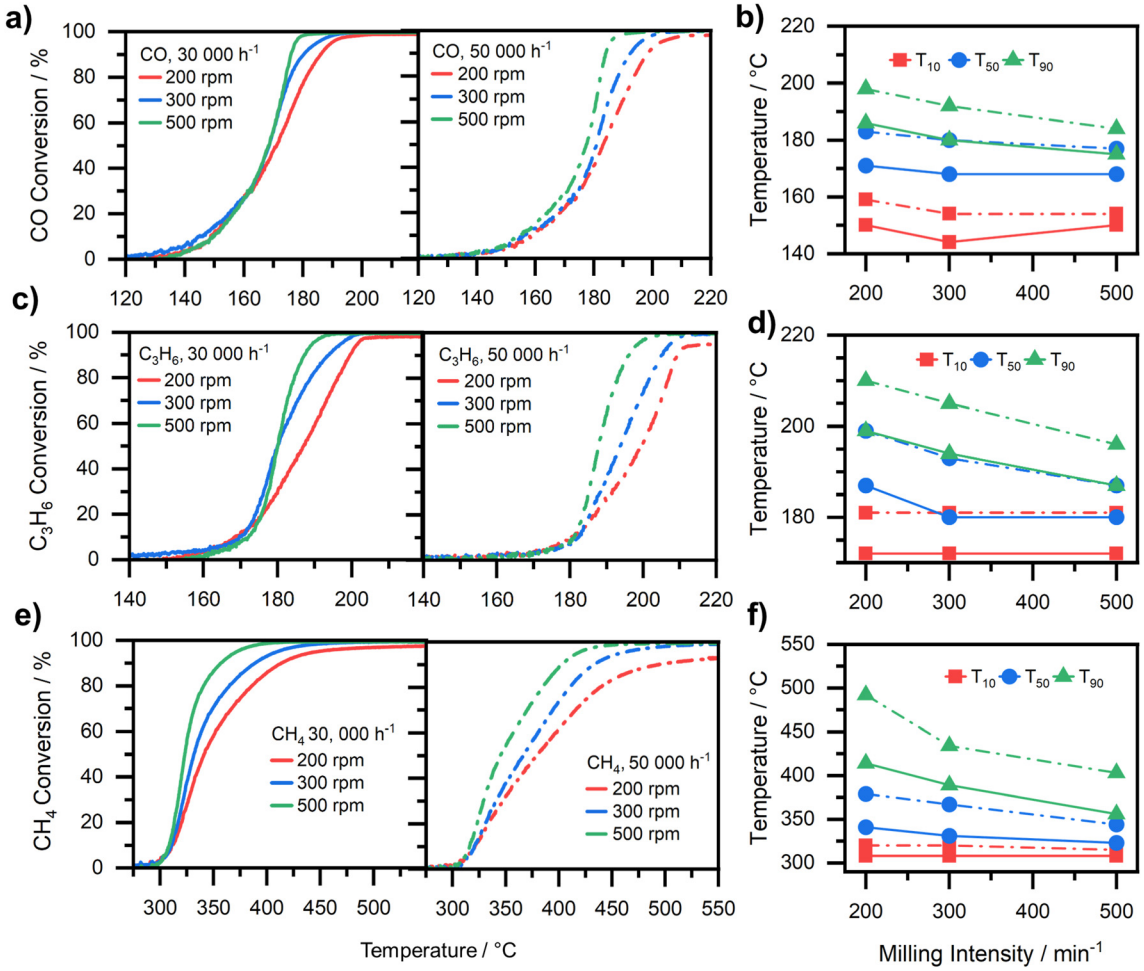

Fig. 7 Catalytic activity for a gas mixture of 3000 ppm CH_4, 500 ppm C_3H_6, and 1000 ppm CO as a function milling intensity with a constant amount of binder of 10 wt%. a) Light-off curves for CO at two different GHSV and b) the corresponding temperatures T_{10}, T_{50} and T_{90}. c) Light-off curves for C_3H_6 at the two different GHSV d) the corresponding temperatures T_{10}, T_{50} and T_{90}. e) Light-off curves for CH_4 at the two different GHSV and f) the corresponding temperatures T_{10}, T_{50} and T_{90}. The lines in the right diagrams are added for guiding purposes.

methane oxidation was investigated in the presence of CO and propylene over the coated Pd-based catalyst under transient conditions. Fig. 7 shows the different light-off curves and the corresponding temperatures at 10% (T_{10}), 50% (T_{50}), and 90% (T_{90}) conversion for the three gaseous pollutants as a function of the applied catalyst milling intensity. Generally, the comparison of different T_{10} as plotted in Fig. 7b), d) and f) for the different gases shows that the conversion in this temperature regime is similar among all samples, only the 200 rpm sample exhibits a slightly higher T_{10}. This indicates the operation of the different samples in the kinetic regime. However, this trend changes when comparing the T_{50} and T_{90} values in Fig. 7b), d) and f) for the different samples. Both temperatures show a similar trend: an increasing milling intensity results in a decrease of T_{50} and T_{90}, but which is more pronounced for T_{90}. Moreover, as can be seen in Fig. 7a), c) and e) the conversion curves of the 200 rpm sample exhibit a "tail" once the temperatures exceed T_{90}, where the catalytic activity increases only slightly with increasing temperature. Notably, even a slight slip of gases is observed, which indicates mass transport limitations, similar to the observation described by R. Pečinka *et al.*[52] We attribute the more pronounced mass transport limitations primarily to the thick average washcoat layer of 230 μm.

Looking more closely at the individual light-off curves for each of the different gases dosed, the trend described before becomes even clearer. For the different samples, the CO conversion curves plotted in Fig. 7a) for a GHSV 30 000 h^{-1} match rather well until a conversion of 35% is reached. The conversion over the 300 rpm and 500 rpm samples is very similar even until reaching roughly 80% conversion. If a GHSV of 50 000 h^{-1} is chosen instead, the curves start to differ from each other already at about 10% CO conversion: the 500 rpm sample shows the highest catalytic activity whereas the 200 rpm sample shows the lowest CO conversion. An analogous observation is made for the oxidation of propylene (Fig. 7c)) and methane (Fig. 7e)), although the slip of hydrocarbons at elevated temperatures becomes even more pronounced than for CO, especially at a GHSV of 50 000 h^{-1} The C–H bond makes CH_4 relatively inert

and non-polar, with a high bond dissociation energy.[53] Hence, the CH_4 conversion starts roughly at 300 °C for all tested samples at a GHSV of 30 000 h^{-1}. They follow the same trend until reaching roughly 10% CH_4 conversion, once again indicating that the catalytic reaction is being operated in the kinetic regime. However, afterwards the catalytic activity steadily decreases with decreasing milling intensity. This trend becomes more pronounced for testing at 50 000 h^{-1}. It is worth noting that not only the light-off curves are shifted to higher temperatures, but also their shape changes significantly, hereby indicating mass transport limitations even for the more active 500 rpm sample. Additionally, the study from Velin *et al.*[54] suggests that especially in the case of methane oxidation these differences of deposited catalyst mass in this regime should barely affect the activity.

To further investigate potential mass transport limitations, methane conversion at T_{50} for the 200 rpm ($T_{50,Pos.1}$ = 339 °C, $T_{50,Pos.2}$ = 344 °C), and 500 rpm ($T_{50,Pos.1}$ = 328 °C, $T_{50,Pos.2}$ = 334 °C) sample was determined along the axial direction of two different channels in a spatially resolved manner (see results in Fig. 8). The onset of methane conversion over the 200 rpm sample is found at a position of approx. 10 mm downstream of the catalyst inlet. After a slight increase until the position of 30 mm, catalytic activity increases almost exponentially towards the outlet. Additionally, the channel at pos. 1 shows a slightly higher activity. In contrast, the 500 rpm sample shows significant CH_4 conversion already after 5 mm. The catalytic activity then steadily increases towards the outlet, with both channels exhibiting an almost identical catalytic activity. Although the capillary-based probing technique applied herein for spatial profiling (SpaciPro) is to some extent invasive as it influences the gas flow,[55] a consistent measurement protocol as chosen herein allows for a direct comparison of the samples. However, it should be pointed out that heat transport limitations cannot be completely excluded for all measurements due to the exothermicity of the methane oxidation reaction in both the case of the SpaciPro and the transient measurements.[56,57] The different alumina particle sizes observed as a function of milling intensity can influence the heat transfer properties of the layer because larger particles increase heat transfer limitations.[58] However, such a behavior is not observed in the SpaciPro measurements, which raises the need for more detailed investigations of heat and mass transport limitations for such a mixtures using a combination of experimental and modelling approaches, including tracking of the temperature along the catalyst channel.

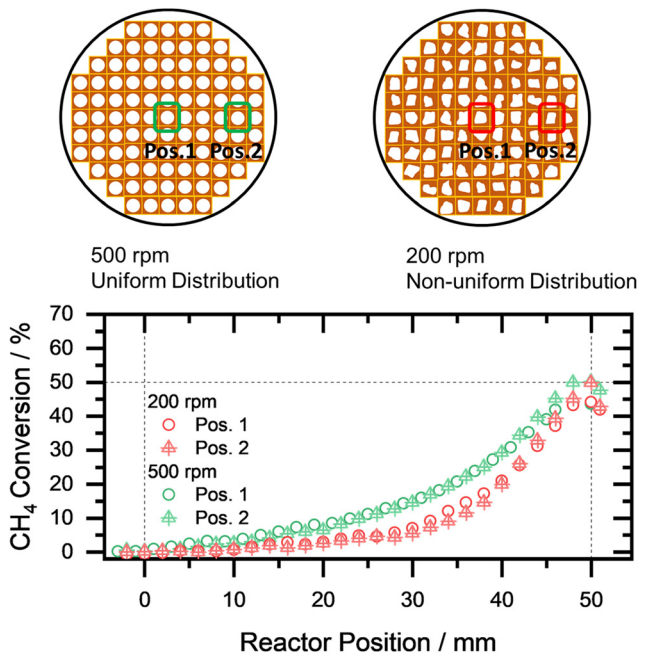

Fig. 8 Spatial profile measurements along the 500 rpm (green) and the 200 rpm (red) sample for two different channels with a GHSV of 30 000 h^{-1} and a gas mixture of 3000 ppm CH_4, 10 vol% O_2 in Ar. The measurements reveal an even conversion in the case of the 500 rpm sample with $T_{50,Pos.1}$ = 328 °C and $T_{50,Pos.2}$ = 334 °C, whereas the 200 rpm sample shows changes in the conversion slope with $T_{50,Pos.1}$ = 339 °C, $T_{50,Pos.2}$ = 344 °C.

The results underscore the importance of the catalyst layer thickness and the homogeneity of the washcoating. In the case of the 200 rpm sample the catalyst layer is a too thick diffusion barrier for the gas to efficiently penetrate into the layer, thus the catalyst layer is not efficiently used. This is also in line with a study by Becher *et al.*[30] on a related reaction, which showed that during operation the reactant gases only penetrated (the upper) 20 μm of the catalyst layer, leaving especially the catalyst washcoat in the corners of the monolith unused at higher temperatures. Also, Groppi *et al.*[59] reported that only 20–50 μm contribute to methane oxidation in Pd-based catalyst (but at higher temperatures and thus higher rates than here). On the other hand, as already observed by the photo-based channel analysis (Fig. 4) the catalyst is non-homogeneously distributed across and along the channels, which reduces the catalytic activity due to mass transfer limitations. The 500 rpm sample on the other hand shows a fairly homogeneous distribution of the catalyst across all channels with thin layers as displayed by the photo-based channel analysis (Fig. 4) and also along the channels confirmed with tomography (Fig. 3). The thin layers lead to a higher catalyst efficiency as methane can penetrate the washcoat and reach also the inner Pd particles, thus resulting in higher catalytic activity already at the inlet of the honeycomb. Hence, the results emphasize the important control of the coating parameter to efficiently use the palladium-based catalyst subject to the present study with the optimized parameters.

These significant differences in the catalytic activity for the different samples stem from a variety of sample properties. It was shown with the diffuse backlight-illumination imaging method that with an increased milling intensity, smaller particles are produced. Smaller particles themselves provide a higher surface to volume ratio, thus improving diffusion properties.[60] Smaller grains offer shorter diffusion distances to and from the active center improving

their catalytic activity. Here it is to be noted that we assume that the meso and micro porosity as well as the phases of the alumina support are not altered during the milling process (Fig. S1†). Hence, the local effective diffusion coefficient inside the particles will be similar, only the diameter of the grains is smaller. However, the overall effective diffusivity trough the coated layers is affected by the milling. Furthermore, the rheological measurements showed that small particles produce a more stable slurry that gave no sign of sedimentation during the duration of the rheological investigation (approx. 4.3×10^{-5} cm h^{-1}, based on Stokes' law). The predominant presence of small particles ensures a homogeneous slurry during the coating process and facilitates less particle movement during the drying process, yielding an even and coherent layer which was also observed by SEM-images (see Fig. 6). After the deposition, the small particles form a thinner and less macroporous layer consisting of significantly smaller macropores. Neglecting the external transport to the catalyst layer, this provides a smaller diffusion barrier as the gas has to pass a thinner layer. This decisive parameter of film thickness and homogeneity can easily be followed by the fast camera analysis. In section 3.1 it was shown that the photo-based method allows a fast tracking of the layer thickness and also of their homogeneity. Those findings can now be coupled with the findings from the activity tests, where it becomes apparent that the measured OCA and a thin catalyst layer are correlated to the achieved catalytic activity. These findings show that a higher OCA, which translates to thin layers, goes along with an increased catalytic activity.

The comparison of the light-offs for the samples with different weight percentages of binder (constant milling intensity of 300 rpm) as depicted in Fig. 9a), c) and e) does not uncover significant variations of the catalytic activity. This becomes even more obvious when comparing the temperatures T_{10}, T_{50} and T_{90} in Fig. 9b), d) and f). Irrespective of the space velocity, negligible differences of only a few centigrade are found for CO and propylene, while

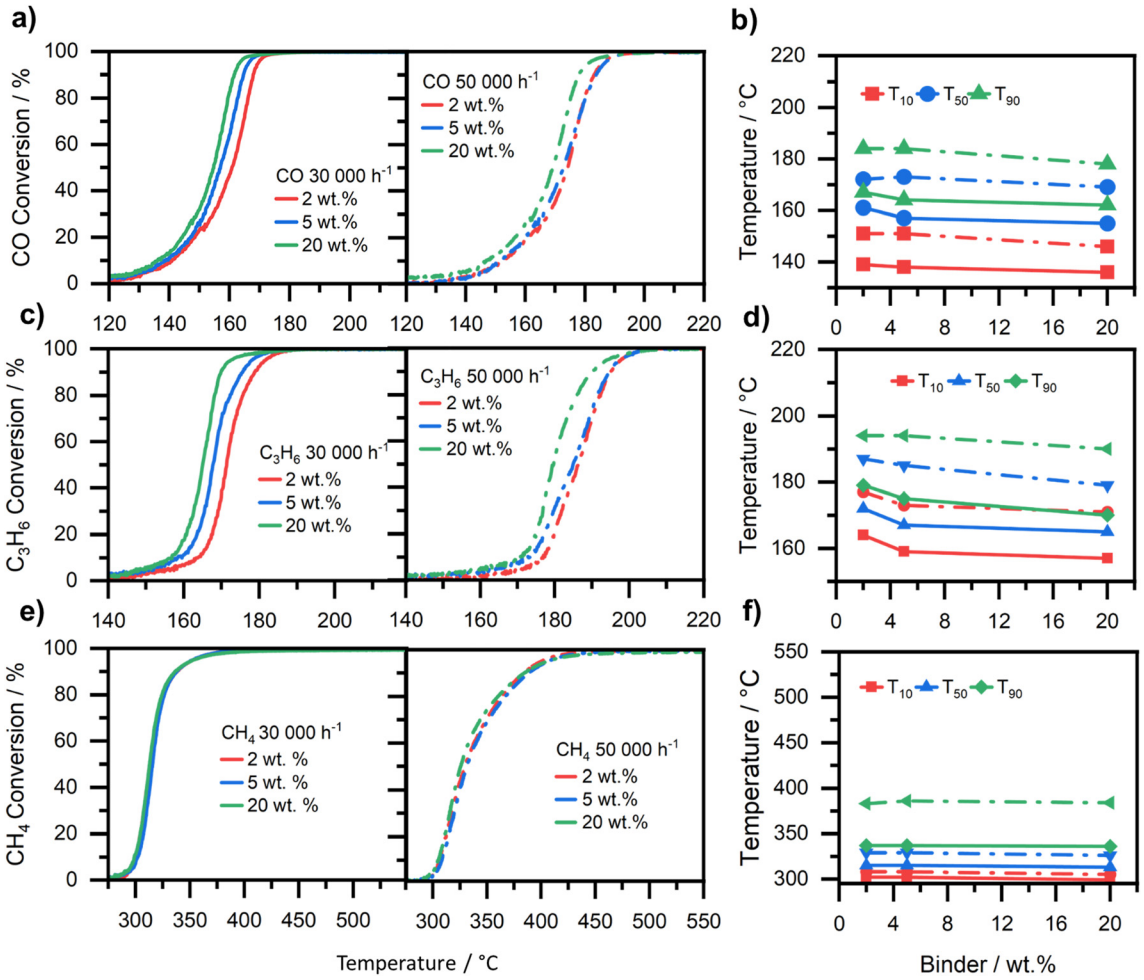

Fig. 9 Catalytic activity for a gas mixture of 3000 ppm CH_4, 500 ppm C_3H_6 and 1000 ppm CO as a function of different binder weight percentages with a constant milling intensity of 300 rpm. a) Light-off curves for CO at the two different GHSV and b) the corresponding temperatures T_{10}, T_{50} and T_{90}. c) Light-off curves for C_3H_6 at the two different GHSV and d) the corresponding temperatures T_{10}, T_{50} and T_{90}. e) Shows the light-off curves for CH_4 at the two different GHSV and f) the corresponding temperatures T_{10}, T_{50} and T_{90}. The lines in the right diagrams are added for guiding purposes.

the temperatures do not vary at all for methane. Hence, further investigation would be required to fully deconvolute the influence on the activity for CO and propylene oxidation. That fact that no relevant activity variations are found matches the observations from the photo-based characterization method, underscoring its high suitability as a fast feedback loop analysis. The analysis for the different samples with different amounts of binder added uncovered only minor differences in OCA (Fig. 4). This implies that the added binder does not directly influence the activity, indicating that there are no phenomena such as blocking of actives sites or blocking of the mesopores *i.e.* not significantly adding to transport limitations. However, the mechanical stability tests (Fig. S2†) show that higher amounts of binder result in an increased mechanical stability, which is a feature of high practical relevance because typical operation conditions impose high mechanical stress on the materials due to (temporarily) high gas flows, thermal expansion, abrasion, or even formation of condensate, *e.g.* water, at lower temperatures.

4. Conclusion

In this work a non-invasive fast feedback loop was established for rapid and reproducible characterization of structured catalysts. For this purpose, a photo-based analysis was developed to help check the quality and thickness of coated monolithic honeycombs, with the benefit of probing all channels from both the in- and outlet perspective, thus increasing the statistics. The suitability of the newly proposed photo-based analysis was then confirmed with the well-established method of lab-based X-ray tomography. For demonstrating its advantages catalytic oxidation of CO, propylene, and methane over Pd-based catalysts was used as example reaction. All results were supplemented by mercury intrusion porosimetry, the diffuse backlight-illumination imaging method, rheological measurements, and SEM-analysis.

Significant changes in the sample characteristics were obtained by systematically varying two key parameters: the catalyst milling intensity and the amount of binder. The increasing milling intensity leads to the formation of smaller particles, providing a colloidally stable slurry. This allowed to prepare a homogenous distribution of catalyst layer, as there was less movement of the Pd/Al_2O_3 particles during the drying step. The small catalyst particles first penetrate the honeycomb structure and then form a coherent thin layer of about 115 μm thickness, whereas insufficiently low milling intensities resulted in larger particles and thus an average layer thickness of up to 230 μm. Thin layers did not only have a higher quality in terms of homogeneity but also exhibited a higher activity due to less diffusion limitation. On the other hand, low milling intensities resulted in lower catalytic activity as the efficiency is decreased due to inhomogeneity of the catalyst layers and larger characteristic length, which led to a more pronounced diffusion limitation. This is reflected by a smaller global reaction rate and the slower increase in conversion at elevated conversions and temperatures. This trend is even more pronounced with 50 000 h^{-1} and increases with gases from CO over propylene to CH_4. In the case of different amounts of binder, it can be observed that there is no significant trend when comparing T_{10}, T_{50}, and T_{90}. However, the binder adds important properties such as mechanical stability during operation. This becomes more relevant at elevated temperatures, higher space velocities, and for use in technical systems where mechanical and other stresses are high. In conclusion, the photo-based channel analysis may not be able to capture all details of the production process, but it allows for a rapid estimation of the washcoat on a lab-scale and thus complements more advanced methods like X-ray tomography or cross-section SEM-EDX images that can only be taken on selected samples.

Data availability

All pictures of the developed photo analysis and tomography will be available free of charge. See DOI: **https://doi.org/10.35097/SIMRazQvMFmcyCnX**.

Conflicts of interest

There are no conflicts to declare.

Acknowledgements

This study was funded by the Deutsche Forschungsgemeinschaft (DFG, German Research Foundation) – SFB 1441 – Project-ID 426888090 (projects B02, C02, C03). The authors would like to thank R. Irvine for their help with the experimental work, I. Zeller (ITCP, KIT) for the SEM-analysis, C. Klein (ITCP, KIT) for the rheological measurements, L. Braun (ITCP, KIT) for the XRD analysis, M. Burcea (CVT, KIT) for the MIP analysis, J. Czechowsky (ITCP, KIT) for his assistance during the catalyst preparation, T. Bergfeldt (IAM-AWP, KIT) for ICP-OES analysis, A. Schucker (IAM-ET, KIT) for her help with the μ-CT analysis, and O. Deutschmann (ITCP, KIT) for provision of infrastructure and equipment for the SpaciPro experiments and the fruitful discussion.

References

1 M. Sajjad and W. Lu, *Electrochem. Sci. Adv.*, 2022, **2**, e202100075.
2 T. C. Le, G. H. Hong, G. Y. Lin, Z. Li, D. Y. H. Pui, Y. L. Liou, B. T. Wang and C. J. Tsai, *Sustainable Environ. Res.*, 2021, **31**, 1–12.
3 S. P. Shukla, C. D. Madhusoodana and R. N. Das, *Key Eng. Mater.*, 2006, **317–318**, 759–764.
4 P. Lott, M. Casapu, J.-D. Grunwaldt and O. Deutschmann, *Appl. Catal., B*, 2024, **340**, 123241.
5 F. Kapteijn and J. A. Moulijn, *Catal. Today*, 2022, **383**, 920–5861.

6 *Structured Catalysts and Reactors*, ed. A. Cybulski and J. A. Moulijn, CRC Taylor & Francis Group, Boca Raton, 2nd edn, 2005, pp. 1–807.
7 Y. Guo, M. Wen, G. Li and T. An, *Appl. Catal., B*, 2021, **281**, 119447.
8 A. Gärtner, T. Lenk, R. Kiemel, S. Casu, C. Breuer and K. Stöwe, *Top. Catal.*, 2016, **59**, 1071–1075.
9 R. Balzarotti, C. Cristiani and L. F. Francis, *Catal. Today*, 2019, **334**, 90–95.
10 L. Giani, C. Cristiani, G. Groppi and E. Tronconi, *Appl. Catal., B*, 2006, **62**, 121–131.
11 F. Mehdipour, T. Delrieux, F. Maurer, J.-D. Grunwaldt, C. Klahn and R. Dittmeyer, *Catal. Commun.*, 2024, 106873.
12 R. Balzarotti, C. Cristiani and L. F. Francis, *Surf. Coat. Technol.*, 2017, **330**, 1–9.
13 V. Claude, J. G. Mahy, T. Lohay, J. Geens and S. D. Lambert, *Processes*, 2022, **10**, 875.
14 D. F. M. Santos, O. S. G. P. Soares, J. L. Figueiredo and M. F. R. Pereira, *Environ. Technol.*, 2021, **42**, 2504–2515.
15 V. Meille, *Appl. Catal., A*, 2006, **315**, 1–17.
16 M. Ambrosetti, R. Balzarotti, C. Cristiani, G. Groppi and E. Tronconi, *Catalysts*, 2018, **8**, 510.
17 R. Balzarotti, M. Ambrosetti, M. Arnesano, A. Anglani, G. Groppi and E. Tronconi, *Appl. Catal., B*, 2021, **283**, 119651.
18 M. C. Bacariza, A. N. Mendes, C. Ozhan, P. Da Costa and C. Henriques, *Ind. Eng. Chem. Res.*, 2019, **58**, 11799–11810.
19 F. Maurer, J. Jelic, J. Wang, A. Gänzler, P. Dolcet, C. Wöll, Y. Wang, F. Studt, M. Casapu and J.-D. Grunwaldt, *Nat. Catal.*, 2020, **3**, 824–833.
20 R. Burch and F. J. Urbano, *Appl. Catal., A*, 1995, **124**, 121–138.
21 O. Deutschmann and J.-D. Grunwaldt, *Chem. Ing. Tech.*, 2013, **85**, 595–617.
22 D. Ciuparu, M. R. Lyubovsky, E. Altman, L. D. Pfefferle and A. Datye, *Catal. Rev.: Sci. Eng.*, 2002, **44**, 593–649.
23 E. J. Peterson, A. T. DeLaRiva, S. Lin, R. S. Johnson, H. Guo, J. T. Miller, J. H. Kwak, C. H. F. Peden, B. Kiefer, L. F. Allard, F. H. Ribeiro and A. K. Datye, *Nat. Commun.*, 2014, **5**, 4885.
24 F. Maurer, A. Gänzler, P. Lott, B. Betz, M. Votsmeier, S. Loridant, P. Vernoux, V. Murzin, B. Bornmann, R. Frahm, O. Deutschmann, M. Casapu and J.-D. Grunwaldt, *Ind. Eng. Chem. Res.*, 2021, **60**, 6662–6675.
25 H. Becker, R. Güttel and T. Turek, *Catal. Sci. Technol.*, 2015, **6**, 275–287.
26 H. Becker, R. Güttel and T. Turek, *Catal. Sci. Technol.*, 2014, **6**, 275.
27 D. Bernsmeier, L. Chuenchom, B. Paul, S. Rümmler, B. Smarsly and R. Kraehnert, *ACS Catal.*, 2016, **6**, 8255–8263.
28 Y. Zhang, Y. Zhou, A. Qiu, Y. Wang, Y. Xu and P. Wu, *Ind. Eng. Chem. Res.*, 2006, **45**, 2213–2219.
29 G. T. Whiting, A. D. Chowdhury, R. Oord, P. Paalanen and B. M. Weckhuysen, *Faraday Discuss.*, 2016, **188**, 369–386.
30 J. Becher, T. L. Sheppard, Y. Fam, S. Baier, W. Wang, D. Wang, S. Kulkarni, T. F. Keller, M. Lyubomirskiy, D. Brueckner, M. Kahnt, A. Schropp, C. G. Schroer and J.-D. Grunwaldt, *J. Phys. Chem. C*, 2019, **123**, 25197–25208.
31 P. E. Dim, R. S. Fletcher and S. P. Rigby, *Chem. Eng. Sci.*, 2016, **140**, 291–298.
32 S. Weber, A. Diaz, M. Holler, A. Schropp, M. Lyubomirskiy, K. L. Abel, M. Kahnt, A. Jeromin, S. Kulkarni, T. F. Keller, R. Gläser, T. L. Sheppard, S. Weber, T. L. Sheppard, A. Diaz and M. Holler, *Adv. Sci.*, 2022, **8**, 2105432.
33 L. Vásárhelyi, Z. Kónya, Á. Kukovecz and R. Vajtai, *Mater. Today Adv.*, 2020, **8**, 100084.
34 V. Novák, M. Dudák, P. Kočí and M. Marek, *Curr. Opin. Chem. Eng.*, 2015, **9**, 16–26.
35 J.-D. Grunwaldt and C. G. Schroer, *Chem. Soc. Rev.*, 2010, **39**, 4741–4753.
36 S. Das, R. Pashminehazar, S. Sharma, S. Weber and T. L. Sheppard, *Chem. Ing. Tech.*, 2022, **94**, 1591–1610.
37 L. Giani, G. Groppi and E. Tronconi, *Ind. Eng. Chem. Res.*, 2005, **44**, 4993–5002.
38 R. Burch, D. J. Crittle and M. J. Hayes, *Catal. Today*, 1999, **47**, 229–234.
39 R. Burch and M. J. Hayes, *J. Mol. Catal. A: Chem.*, 1995, **100**, 13–33.
40 S. Brunauer, P. H. Emmett and E. Teller, *J. Am. Chem. Soc.*, 1938, **60**, 309–319.
41 E. P. Barrett, L. G. Joyner and P. P. Halenda, *J. Am. Chem. Soc.*, 1951, **73**, 373–380.
42 J. Li, S. Shao and J. Hong, *Meas. Sci. Technol.*, 2020, **32**, 015406.
43 M. Lausch, P. Brockmann, F. Schmitt, B. J. M. Etzold and J. Hussong, *Chem. Eng. Sci.*, 2024, **289**, 119864.
44 T. Günter, J. Pesek, K. Schäfer, A. Bertótiné Abai, M. Casapu, O. Deutschmann and J.-D. Grunwaldt, *Appl. Catal., B*, 2016, **198**, 548–557.
45 K. A. Karinshak, P. Lott, M. P. Harold and O. Deutschmann, *ChemCatChem*, 2020, **12**, 3712–3720.
46 C. Diehm and O. Deutschmann, *Int. J. Hydrogen Energy*, 2014, **39**, 17998–18004.
47 J. Schindelin, I. Arganda-Carreras, E. Frise, V. Kaynig, M. Longair, T. Pietzsch, S. Preibisch, C. Rueden, S. Saalfeld, B. Schmid, J. Y. Tinevez, D. J. White, V. Hartenstein, K. Eliceiri, P. Tomancak and A. Cardona, *Nat. Methods*, 2012, **9**, 676–682.
48 M. J. Stutz and D. Poulikakos, *Chem. Eng. Sci.*, 2008, **63**, 1761–1770.
49 M. Sabharwal and M. Secanell, *Electrochim. Acta*, 2022, **419**, 140410.
50 Z. Qie, A. Rabbani, Y. Liang, F. Sun, J. Behnsen, Y. Wang, S. Wang, Y. Zhang, H. Alhassawi, J. Gao, G. Zhao, M. Babaei, A. A. Garforth, Y. Jiao and X. Fan, *Chem. Eng. J.*, 2022, **440**, 135843.
51 M. Blažek, M. Žalud, P. Kočí, A. York, C. M. Schlepütz, M. Stampanoni and V. Novák, *Chem. Eng. J.*, 2021, **409**, 128057.
52 R. Pečinka, M. Blažek, R. Knopp, P. Kočí and A. York, *Chem. Eng. Sci.*, 2022, **260**, 117876.

53 A. Caballero and P. J. Pérez, *Chem. Soc. Rev.*, 2013, **42**, 8809–8820.
54 P. Velin, C. R. Florén, M. Skoglundh, A. Raj, D. Thompsett, G. Smedler and P. A. Carlsson, *Catal. Sci. Technol.*, 2020, **10**, 5460–5469.
55 M. Hettel, C. Diehm, B. Torkashvand and O. Deutschmann, *Catal. Today*, 2013, **216**, 2–10.
56 W. Lang, P. Laing, Y. Cheng, C. Hubbard and M. P. Harold, *Appl. Catal., B*, 2017, **218**, 430–442.
57 J.-D. Grunwaldt, M. Maciejewski and A. Baiker, *Phys. Chem. Chem. Phys.*, 2003, **5**, 1481–1488.
58 T. F. McKenna, R. Spitz and D. Cokljat, *AIChE J.*, 1999, **45**, 2392–2410.
59 G. Groppi, W. Ibashi, E. Tronconi and P. Forzatti, *Catal. Today*, 2001, **69**, 399–408.
60 L. Jiang, W. Zhu, C. Wang, W. Dong, L. Zhang, G. Wang, B. Chen, C. Li and X. Zhang, *Appl. Catal., B*, 2016, **180**, 344–350.